

SUBPIXEL LOCALIZATION OF OPTICAL VORTICES USING ARTIFICIAL NEURAL NETWORKS

Agnieszka Popiołek-Masajada¹⁾, Ewa Frączek²⁾, Emilia Burnecka¹⁾

1) Wrocław University of Science and Technology, Faculty of Fundamental Problems of Technology, Department of Optics and Photonics, Poland (agnieszka.masajada@pwr.edu.pl)

2) Wrocław University of Science and Technology, Department of Telecommunication and Teleinformatics, Poland (✉ ewa.fraczek@pwr.edu.pl, +48 71 320 30 84)

Abstract

Optical vortices are getting attention in modern optical metrology. Because of their unique features, they can be used as precise position markers. In this paper, we show that an artificial neural network can be used to improve vortex localization. A deep neural network with several hidden layers was trained to find subpixel vortex positions on the spiral phase maps. Several thousand training samples, differing by spiral density, its orientation, and vortex position, were generated numerically for teaching purposes. As a result, Best Validation Performance of the order of 10^{-5} pixel has been reached. To verify the usefulness of the proposed method, a related experiment in the setup of an optical vortex scanning microscope has been reported. It is shown that the vortex can be localized with subpixel accuracy also on experimental phase maps.

Keywords: optical vortex, spiral phase map, pseudo phase, deep learning, neural network.

© 2021 Polish Academy of Sciences. All rights reserved

1. Introduction

Light fields in classical optics are characterized by amplitude, phase, and polarization state. Nowadays many exotic optical fields can be produced with help of modern optical equipment, which allows modulation of their amplitude and phase. An interesting example is a field carrying optical vortices [1–3]. An optical vortex is a singular phase structure having a point to which the equiphase lines converge (vortex point). They attract attention in modern optical metrology because they are stable structures having a characteristic point of zero intensity (at the vortex point) and can serve as precise position markers. On the other hand, they are well-defined points on the phase map and can be localized with arbitrary accuracy, at least in theory. Several approaches to apply optical vortices in metrology have been proposed in different areas of optics so far. For instance, they were used as encoders for position marking in displacement metrology [4, 5]. Speckle patterns appear as a result of interference of many waves having different

phases and amplitudes. Each dark spot in a speckle field contains an optical vortex. These vortices can be uniquely identified by their internal structure and used to measure some dynamic phenomena in fluids or on the solid sample surface. For example, tracing vortex movement caused object by displacement enables to determine this displacement with high accuracy. Optical vortices can be also used as phase markers in optical vortex interferometry [6–8]. Tracing a change in their position in the vortex lattice enables recovering the phase shift introduced into the object beam. An interesting application of vortex structure are topography measurements [9, 10]. Here, the measured surface is mapped into an array of vortex points and surface depth is reconstructed from angular rotation of the vortex point spread function assigned to the measuring points. In High-Resolution Interference Microscopy [11, 12] singularities are born in the field scattered or transmitted by nanostructures. Detecting them allows for its characterization and positioning. A light beam with the internal vortex phase structure can serve as a kind of scanning tool. As a result of its interaction, the microscopic sample causes changes in vortex localization within the beam. That can be used to characterize a sample's feature or position [13–15].

In the presented manuscript we investigate, for the first time, whether artificial neural networks can be applied to enhance vortex localization in vortex metrology. Deep learning technology has been widely utilized in image recognition. In the case of vortex beam, it has been used to recognize its different spatial modes [16] or to differentiate between nearby spatial vortex states [17, 18]. In our work, we trained a neural network with help of numerically generated spiral phase maps of different spiral densities [19], orientations, and positions. From the training set a high value of Best Validation Performance was reached which showed that vortex position can be found with subpixel accuracy. Then this algorithm has been used to find the vortex position in the Optical Vortex Scanning Microscope – a novel optical instrument we proposed in our previous papers [20–22]. The main idea of this instrument is to use a vortex as a scanning point. The optical vortex here was introduced into the laser beam via the *spiral phase plate* (SPP) mounted on the piezo stage. That enabled its shifting in the direction perpendicular to the optical axis. As a result, vortex embedded in the beam was also shifted. Next, the vortex beam was focused by a microscope objective and, in this way, a reduction of the vortex shift range was achieved. The reduction rate depends on the objective power/magnification. A focused spot then was observed on the CCD camera through the imaging system. If SPP is shifted by a very small step, then the vortex observed on the CCD will be shifted within one camera pixel. Our previous vortex localization procedures positioned it with the accuracy of one pixel. In this paper, we show that an artificial neural network will improve this accuracy to 1/4 pixel.

2. Methodology

2.1. Vortex beam phase map description

One of the natural solutions of the paraxial wave equation is helical wave which can be described in terms of the Laguerre–Gaussian mode. It contains the $\exp(im\phi)$ phase term which describes the phase vortex of topological charge m . The mathematical form of the complex amplitude of such beam can be expressed in cylindrical coordinates (r, ϕ, z) by the equation:

$$U_{LG}(r, \phi, z) = E_0 \frac{w_0}{w} \left(\frac{r}{w}\right)^{|m|} \exp\left(-\frac{r^2}{w^2}\right) \exp\left[-i\left(m\phi + \frac{kr^2}{2R} + kz + \Phi_G\right)\right], \quad (1)$$

where w_0 refers to the beam waist, $w(z) = w_0 \sqrt{1 + \frac{z^2}{z_R^2}}$ is the transverse beam radius, $R(z) = z \left(1 + \frac{z_R^2}{z^2} \right)$ is the radius of curvature of the beam wavefront, $z_R = \frac{kw_0^2}{2}$ is the Rayleigh range and $\Phi_G(z)$ is the Gouy phase. At the fixed observation plane z , the intensity and phase maps reveal characteristic features shown in Fig. 1. In the intensity picture, there is a characteristic bright ring pattern (Fig. 1a). The phase picture reveals a spiral character (Fig. 1b). The end of the spiral on the phase map indicates the position of the vortex point and is associated with the zero intensity point. We will consider the beam with the topological charge $m = 1$.

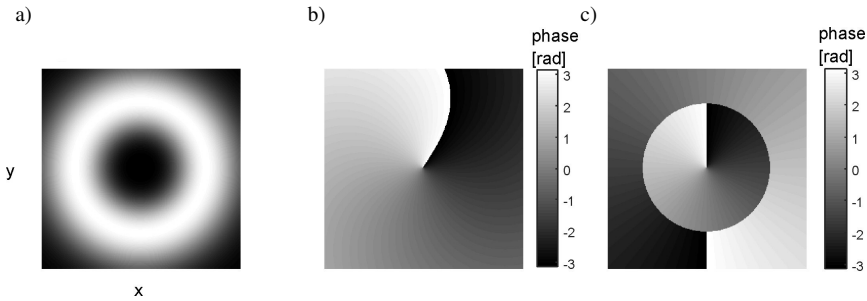


Fig. 1. Vortex beam: a) intensity, b) phase plotted as $\arg(U_{LG})$, c) pseudo phase, plotted as $\arg(\tilde{I}(x, y))$ from (4).

The spiral seen on the phase map can have different numbers of turns and orientations, depending on wavefront curvature or phase connected with beam propagation.

The spiral feature of the vortex beam phase in the experimental conditions can be extracted from the interferograms via the Fourier methods [23]. In the case when it is not possible to construct an interferometer which generates characteristic fork interference fringes, one can apply the Laguerre–Gauss filter operation to intensity image and get so-called complex signal $\tilde{I}(x, y)$ [5, 24]:

$$\tilde{I}(x, y) = \int_{-\infty}^{+\infty} \int_{-\infty}^{+\infty} LG(f_x, f_y) \cdot FI(f_x, f_y) \exp \{ 2\pi i (f_x x + f_y y) \} df_x df_y, \quad (2)$$

where $FI(f_x, f_y)$ is a Fourier transform of the intensity image. Filter $LG(f_x, f_y)$ is defined as:

$$LG(f_x, f_y) = (f_x + if_y) \exp \left(-\frac{f_x^2 + f_y^2}{d^2} \right) = \rho \cdot \exp \left(-\frac{\rho^2}{d^2} \right) \cdot \exp(i\theta), \quad (3)$$

where $\rho = \sqrt{f_x^2 + f_y^2}$ and $\theta = \arctan(f_x/f_y)$ and d serves as a bandwidth of the LG filter. Results obtained by the operation (2) can be generally written as

$$I(x, y) \rightarrow \tilde{I}(x, y) = \left| \tilde{I}(x, y) \right| \exp [i\phi(x, y)] = I(x, y) \otimes FTLG(x, y), \quad (4)$$

here \otimes denotes convolution, $\phi(x, y)$ is called the pseudo phase, $FTLG(x, y)$ is the Laguerre–Gauss function in the spatial domain (inverse Fourier transform of (3)) and can be written as [5]:

$$FTLG(x, y) = i \cdot \pi^2 d^4 \cdot r \cdot \exp \left(-\pi^2 r^2 d^2 \right) \cdot \exp(i\phi). \quad (5)$$

An exemplary pseudo-phase map obtained by performing convolution operation described by (4) is presented in Fig. 1c.

2.2. Vortex localization

The localization of the vortex point was carried out by finding the end of the spiral phase line on the phase map. Figure 2 (upper left) shows the central part of the phase distribution with the cross-marked position of the vortex point. Our present localization procedures point out the approximate position of the spiral end. Then it takes a few pixels around and tests the way the phase is changing while going around each pixel. It looks for the characteristics phase changes pattern. We call this method *Spiral End Detection* (SED). This method indicates the vortex position and gives a standard deviation of 1.5 pixels which gives localization accuracy equal to 3 pixels. The other phase maps in Fig. 2 are plotted for four different vortex shift cases. Vortex was shifted down by 0.25, 0.5, 0.75, and 1 pixel from the initial position. In the case of a shift by a distance smaller than 1 pixel, our localization procedures indicated the same vortex position on the phase map (marked by cross symbol). At the first sight, the phase maps look the same. However, if we inspect the phase values in the vicinity of this point, we observe that it changes as the vortex point is moved. This fact is illustrated by the numbers shown below the phase maps in Fig. 2 and on the bottom plot. This subtle phase change in the close vicinity of the vortex point is a clue for the neural network for its more accurate localization. The input data for the artificial neural network was a 20×20 pixel image of the phase map section. A fragment of the phase map was chosen, so that the vortex point was in the centre of the image. The optical vortex on the numerically generated phase map was of a size comparable to the experimentally detected one.

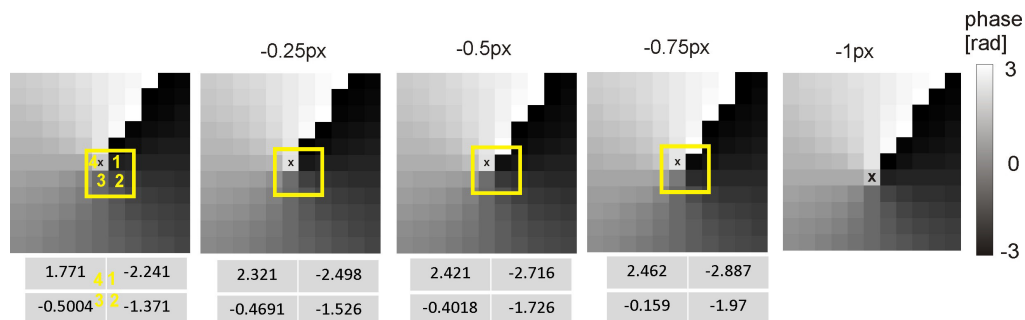


Fig. 2. Part of the phase map containing optical vortex. The black cross indicates the vortex position found by our initial localization procedures. On subsequent maps to the right, a vortex was shifted down by 0.25, 0.5, 0.75, and 1 pixel. In the case of a shift smaller than 1 pixel, the localization procedure pointed out the same position on the phase map. Numbers below the phase maps show the phase values at points 1, 2, 3, 4. Despite finding the same position of the vortex point with the localization procedure, the phase in the vicinity of the localized point changes.

2.3. Deep learning

Artificial neural networks are often used to solve problems which are difficult to solve using standard programming methods. In general, a neural network contains an input layer and an output layer composed of artificial neurons, with hidden layers in between, as shown schematically in Fig. 3. A neural network with the number of hidden layers bigger than 1 is called a deep neural network. Each neuron applies a nonlinear transformation on its weighted and biased input, then applies an activation function before the feed-forward process to the next layer of neurons. A learning algorithm is then used to back-propagate the error, which results in the network's ability to learn.

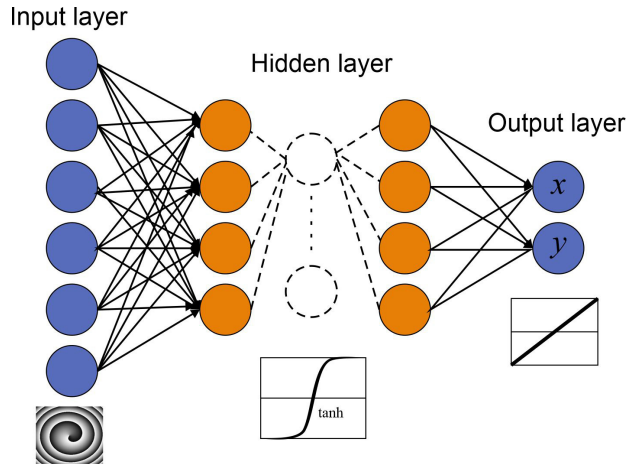


Fig. 3. Scheme of a deep neural network which has hidden layers.

This work uses a feedforward artificial neural network technique with several hidden layers. The hidden layers had the hyperbolic tangent activation function and the output layer was characterized by a linear activation function. The Levenberg–Marquardt algorithm was used to train the network. The tested networks had 400 input neurons for 20×20 pixel phase maps. The designed neural networks had from 1 to 4 hidden layers. All tested networks had two output neurons corresponding to the x and y coordinates of the localized optical vortex [25]. The diagram of the tested networks is shown in Fig. 3.

In this work, we used a relatively simple structure of a neural network which does not require high computing power. Phase maps for teaching and testing purposes were obtained from numerical simulations, which correspond to an image register with a $3.5 \mu\text{m}$ pixel size CCD camera. Several thousand phase map distributions with different features were generated as samples for teaching purposes, differing by the density of the spiral, its rotation, and positions of the vortex point relative to the center of the phase map. The numerically generated training samples were also disturbed by noise and blurring which simulated detector vibration in the experimental set-up. Figure 4 shows several examples of phase maps included in the training set.

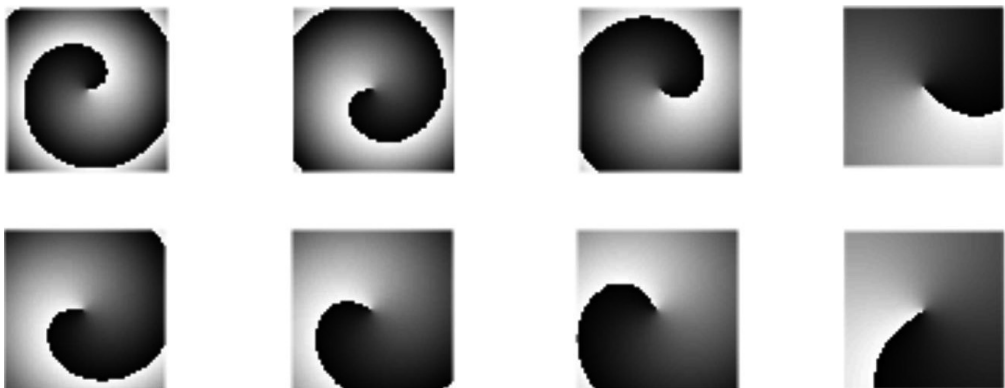


Fig. 4. Sample phase maps for different densities and rotation of the spiral.

Learning samples included Laguerre–Gauss modes with topological charge 1 and Bessel-Gauss modes. With separate tests made on sets containing these two types of modes, no difference was observed in the location accuracy of the optical vortices. This lack of differences is because only small areas around the vortex point were analyzed. All trained artificial neural networks had an input layer with 400 neurons and an output layer with 2 neurons. Tests started using an artificial neural network with one hidden layer. Next, networks with two and three hidden layers were checked. Applying such a configuration for deep learning has significantly reduced the learning time of the neural network and improved the localization accuracy. For the analysis, two networks were selected which had acceptable levels of the BVP (*Best Validation Performance*) parameter. The neuron network with two hidden layers, after 19 learning epochs on the training sample discussed above with 75,000 phase maps, reached $BVP = 5.1e-5$ pixel (Fig. 5a). In the first hidden layer there were 36 neurons, and in the second – 20, which we denote as [36 20]. With the same training sample, the neuron network with three hidden layers [36 20 10], after 25 epochs, reached $BVP = 2.62e-5$ pixel.

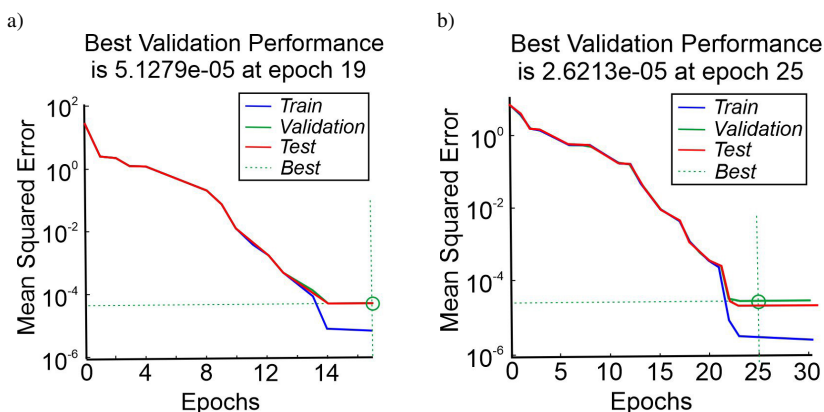


Fig. 5. Vortex point localization accuracy plot for networks with a) two hidden layers [36 20], b) three hidden layers [36 20 10].

In the next step, we tested the neural network localization procedure numerically. The vortex point was shifted in the x -direction by a step equal to 0.1 pixel. Figure 6 shows the central part of the phase maps (plotted area 4×4 pixels around the initial vortex localization) in the case of five different sub-pixel shifts of the vortex point. Additionally, the vortex point position as found by our spiral end detection (triangle) and neural network localization (circle) is shown there. One can see that the SED localization procedure indicates the same pixel on the phase maps (triangle) while the points found by the neural network (circle) shift gradually with the vortex shift. Figure 7

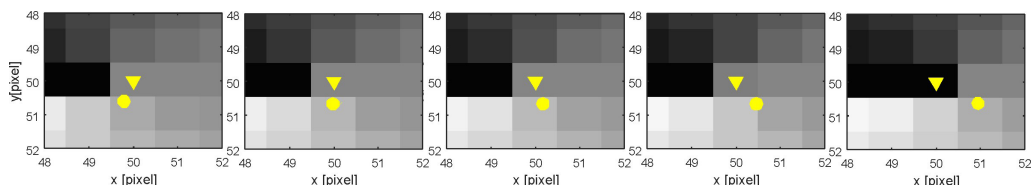


Fig. 6. Central part of the phase maps in case of sub-pixel vortex position. Vortex point position localized with initial localization procedure (triangle) and neural network (circle) are pointed out.

compares the results. The vortex was shifted by 5 pixels from its starting position (50, 50) with the step of 0.1 pixel, which is shown on the horizontal axis. The calculated vortex position is plotted on the vertical axis. We can observe that the vortex point found with the help of the SED localization algorithm (crosses in Fig. 7) forms steps indicating a lack of vortex shift within the subpixel area. There are 10 points on the step corresponding to 0.1 pixel shift. The same analysis but with the vortex point found with the help of a neural network is plotted by circles in Fig. 7. The position of the vortex point indicated by the neural network shifts linearly with the vortex point shift, and no steps, in this case, are observed. Both neural networks produced the same results.

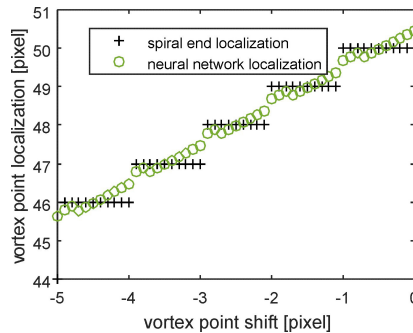


Fig. 7. Comparison of vortex point localization: crosses – spiral end detection, circles – neural network localization (both networks produced similar results).

3. Experimental results

Now we turn to demonstrate the vortex localization on the experimentally detected phase maps. We note here that an artificial network was trained on the simulated images, on which vortex position was precisely known. The phase images were detected in the experimental system shown in Fig. 8. A Gaussian laser beam from a He–Ne laser (632.8 nm) passed through the spiral phase plate which embedded the vortex structure into the beam. SPP was mounted on a piezo

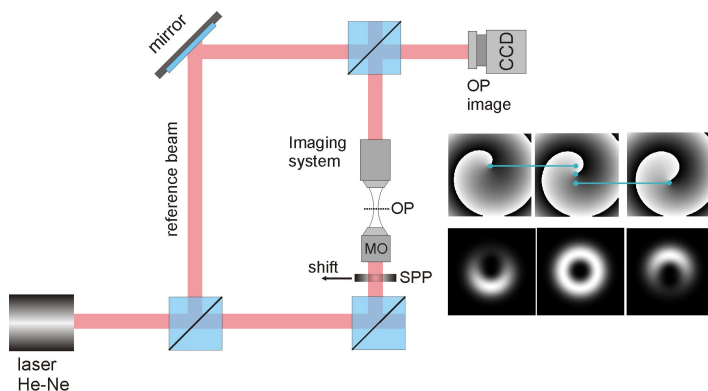


Fig. 8. Scheme of the experimental setup. SPP-spiral phase plate mounted on the piezo stage enabling the transverse shift with small steps, MO – microscope objective, OP – observation plane is imaged via the imaging system onto the CCD camera. With the SPP shift, the vortex point is moved inside the beam. Exemplary phase maps are also shown.

stage which enabled the shift of the vortex in the transverse direction by some distance with a step which could be varied. Next, the vortex beam was focused on by the microscope objective MO. At the observation plane OP vortex point was transversally moved as the SPP was shifted, but at a reduced distance compared to the real SPP shift. The exemplary intensity and phase maps are shown in Fig. 8. The trace of vortex points position forms a vortex trajectory which is a straight line as the SPP is shifted along straight line [20]. The beam size illuminating the MO (20× magnification) was 650 μm and the spot size at the OP was about 3 μm, so the trajectory length was reduced about 216 times. The OP plane is imaged onto the CCD camera (pixel size 5.85 μm) through the imaging system of 220× magnification. An analytical model of this system had been presented in our previous work [20] and it was shown there that its experimental presentation fit well with the analytical solution.

We studied two kinds of images registered in the experimental setup. In the first one reference beam was added to generate interference fringes. Standard Fourier techniques were applied to interferograms to recover the phase maps. In the second one only spot images (without a reference beam) were detected which made the experimental set-up much simpler. These intensity images were transformed to pseudo-amplitude images via the Laguerre–Gauss filters as was pointed out in Section 2.1. A comparison of the phase maps recovered using both methods together with the depicted trajectory (yellow circles) is shown in Fig. 9.

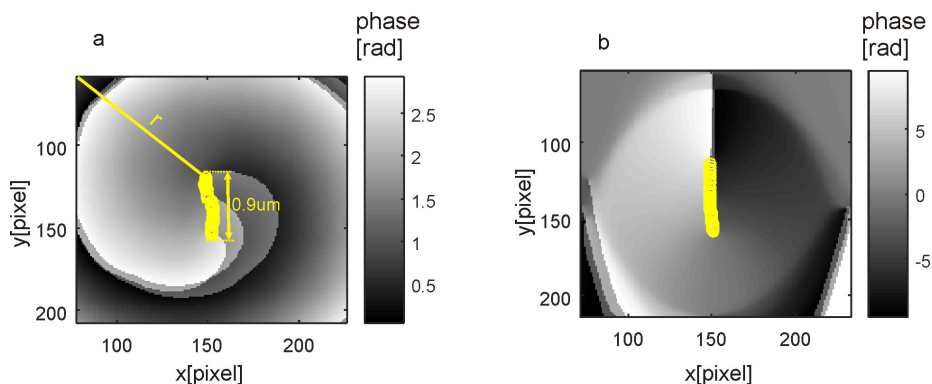


Fig. 9. Phase maps recovered from the experimental set-up. a) from an interferogram, b) from spot images via the Laguerre–Gauss filter. At the observation plane (OP, see Fig. 8), the range of the vortex trajectory was 0.9 μm and the distance between subsequent positions was 26 nm.

When the SPP is shifted by a relatively large step then the observed subsequent vortex positions are separated and detected on different pixels of the camera. Exemplary results of such trajectories are presented in Fig. 10. It shows the radial positions r (see Fig. 9a) of the vortex points versus the SPP shift. In Fig. 10a the SPP was shifted with the step 6 μm over the distance of 0.2 mm which was reduced to 0.9 μm at the OP (Fig. 8). In this case, looking through the imaging system, the subsequent vortex positions were detected on the neighboring pixels on the CCD camera. We calibrated the system with a micrometer target and we found this distance (at the OP) equal to 26 nm. In the case of a tighter SPP step shift (Fig. 10b, step 0.9 μm), the detected subsequent vortex positions are smaller than the distance between the neighboring pixels on the CCD camera, so our SED localization procedure put them in the same position which manifests as step-line in Fig. 10b (similarly as in Fig. 7). The step line distance here is 26nm which is the smallest vortex displacement we can see in this set-up configuration. Figures 10a–b were plotted for the vortex points found from the interferogram–reconstructed phase maps. A similar analysis for

pseudo-phase maps is shown in Fig. 10c–d. In Fig. 10b and Fig. 10d subsequent vortex positions are connected by a line which illustrates experimental noise resulting from set-up vibration. The change of the vortex position resulting from noise is not higher than 1 pixel. When comparing vortex position obtained from both kinds of phase maps (taken from interferogram and pseudo amplitude), we observed 3-pixel vortex discrepancy when the vortex point was at the maximum off-axis position (the pseudo-phase method indicated a vortex shift bigger than resulting from the interferogram). For the central vortex position, however, the SED procedure indicated a vortex point in the same position on both phase maps.

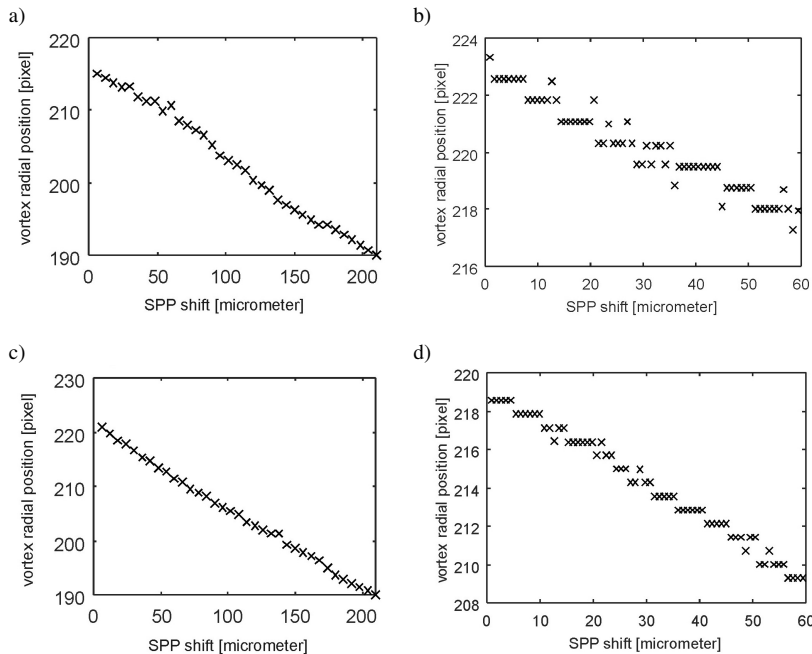


Fig. 10. Vortex trajectory at the OP resulting from the SPP transverse shift plotted as a radial position of the vortex point on the phase maps (from Fig. 9a) versus the SPP shift. a) SPP step shift equal to 6 μm ; b) SPP step shift equal to 0.9 μm (central part of the trajectory shown only). c)–d) the same but for pseudo phase (Fig. 9b).

The results shown in Fig. 10b, Fig. 10d indicate the need to localize vortex points with sub-pixel accuracy. Two types of neural networks described in Section 2.3 were used to investigate the experimentally recorded data. To show the effectiveness of this approach we analyzed images detected for the smaller SPP shift only (0.9 μm). Unfortunately, for some experimental phase maps, a neural network with two layers produced false results. But the three-layer network worked correctly in all cases we analyzed. Green circles plotted in Fig. 11 represent the vortex position found by a neural network. They were plotted together with the vortex positions (crosses) found by the spiral end detection algorithm. We can observe that the neural network algorithm is able “to see” a much smaller vortex shift than resulting from our old procedure. In Fig. 11 one can find 4–5 points at one step (4–5 vortexes on the same pixel on the CCD camera) as detected by spiral end localization. Neural network localization can distinguish these subsequent positions, giving localization accuracy of 1/4 pixel. The accuracy of vortex point detection by neural networks in the experiment is at a level sufficient to detect the noise of the measurement system.

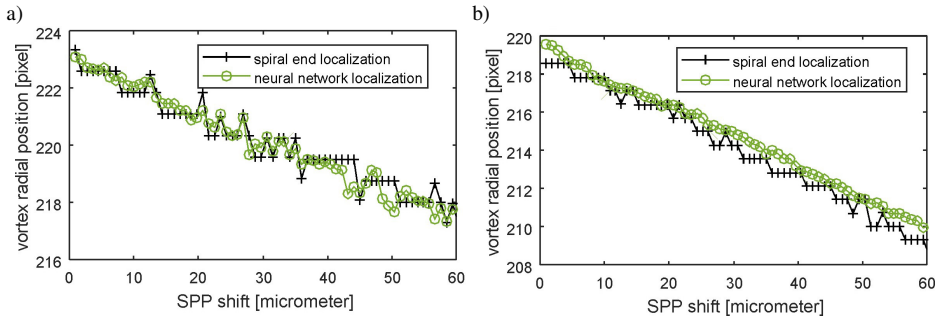


Fig. 11. Comparison of spiral edge detection (crosses) and neural network (circles) localization in experimental conditions, a) phase maps obtained from interferograms, b) phase maps obtained from pseudo-phase images.

4. Conclusions

In this manuscript we demonstrated the ability of deep neural networks to localize vortex points with subpixel accuracy. Two networks which had acceptable levels of the Best Validation Performance parameter, have been selected for vortex localization purposes. Two layers ([36 20]) and three-layers ([36 20 10]) network obtained very high accuracy of the order of 10^{-5} pixel. These networks have been tested on numerically generated images representing the phase maps obtained with an Optical Vortex Scanning Microscope and both of them provided the same, very accurate localization results. In the next step deep learning was applied to the phase maps obtained in the experimental conditions. In this way, two kinds of phase maps have been obtained: one recovered from the interferograms and the other recovered from the intensity images via the spiral transform. The three-layer neural network works properly for all detected phase maps. In experimental conditions, the subpixel vortex shift was obtained by transverse shifting of the SPP within the laser beam and by its constriction (via the microscope objective). The obtained experimental results confirm the ones obtained from computer simulations. The numerical algorithm confirms the accuracy of the vortex point locations at the sub-pixel level with the Best Validation Performance of 10^{-5} pixel. Moreover, the algorithm based on neural networks is less sensitive to experimental disturbances related to wavefront noise. Noise which causes the phase difference on the pitch between the extreme values is smaller than errors resulting from finding the edge of the spiral. Contrary to this, neural networks give accurate results for such noises.

References

- [1] Gbur, G. (2016). *Singular Optics*. CRC Press. <https://doi.org/10.1201/9781315374260>
- [2] Vasnetsov, M. & Staliunas, K. (1999). *Optical vortices*. Nova Science.
- [3] Andrews, D. (2008). *Structured light and its applications*, Academic Press.
- [4] Wang, W., Ishii, N., Hanson, S., Miyamoto, Y., & Takeda, M. (2005). Pseudophase information from the complex analytic signal of speckle fields and its applications. Part II: Statistical properties of the analytic signal of a white-light speckle pattern applied to the microdisplacement measurement. *Applied Optics*, 44(23), 4916–4921. <https://doi.org/10.1364/AO.44.004916>
- [5] Wang, W., Yokozeki, T., Ishijima, R., & Takeda, M. (2006). Optical vortex metrology based on the core structures of phase singularities in Laguerre- Gauss transform of a speckle pattern. *Optics Express*, 14(22), 10195–10206. <https://doi.org/10.1364/OE.14.010195>

- [6] Popiołek-Masajada, A., Borwinska, M., & Frączek, W. (2006). Testing a new method for small-angle rotation measurements with the optical vortex interferometer. *Measurement Science and Technology*, 17(4), 653–658. <https://doi.org/10.1088/0957-0233/17/4/007>
- [7] Frączek E., & Mroczka, J. (2009). An accuracy analysis of small angle measurement using the optical vortex interferometer. *Metrology and Measurement System*, 15(1), 3–8.
- [8] Eastwood, S. A., Bishop, A. I., Petersen, T. C., Paganin, D. M., & Morgan, M. J. (2012). Phase measurement using an optical vortex lattice produced with a three-beam interferometer. *Optics Express*, 20(13), 13947–13957. <https://doi.org/10.1364/OE.20.013947>
- [9] Bouchal, P., Štrbková, L., Dostál, Z., & Bouchal, Z. (2017). Vortex topographic microscopy for full-field reference-free imaging and testing. *Optics Express*, 25(18), 21428–21443. <https://doi.org/10.1364/OE.25.021428>
- [10] Schovaneck, P., Bouchal, P., & Bouchal, Z. (2020). Optical topography of rough surfaces using vortex localization of fluorescent markers. *Optics Letters*, 45(16), 4468–4471. <https://doi.org/10.1364/OL.392072>
- [11] Rockstuhl, C., Märki, I., Scharf, T., Salt, M., Herzig, H. P., & Dändliker, R. (2006). High Resolution Interference Microscopy: A Tool for Probing Optical Waves in the Far-Field on a Nanometric Length Scale, *Current Nanoscience*, 2(4), 337–350. <https://doi.org/10.2174/157341306778699383>
- [12] Symeonidis, M., Nakagawa, W., Kim, D. C., Hermerschmidt, A., & Scharf, T. (2019). High-resolution interference microscopy of binary phase diffractive optical elements. *OSA Continuum*, 2(9), 2496–2510. <https://doi.org/10.1364/OSAC.2.002496>
- [13] Spektor, B., Normatov, A., & Shamir, J. (2008). Singular beam microscopy. *Applied Optics*, 47(4), A78–A87. <https://doi.org/10.1364/AO.47.000A78>
- [14] Masajada, J., Leniec, M., Drobczyński, S., Thienpont, H., & Kress, B. (2009). Micro-step localization using double charge optical vortex interferometer. *Optics Express*, 17(18), 16144–1615. <https://doi.org/10.1364/OE.17.016144>
- [15] Serrano-Trujillo, A., & Anderson, M. E. (2018). Surface profilometry using vortex beams generated with a spatial light modulator. *Optics Communications*, 427, 557–562. <https://doi.org/10.1016/j.optcom.2018.07.003>
- [16] Doster, T., & Watnik, A. T. (2017). Machine learning approach to OAM beam demultiplexing via convolutional neural networks. *Applied Optics*, 56(12), 3386–3396. <https://doi.org/10.1364/AO.56.003386>
- [17] Zhao, Q., Hao, S., Wang, Y., Wang, L., Wan, X., & Xu, C. (2018). Mode detection of misaligned orbital angular momentum beams based on convolutional neural network. *Applied Optics*, 57(35), 10152–10158. <https://doi.org/10.1364/AO.57.010152>
- [18] Knutson, M., Lohani, S., Danac, O., Huver, S. D., & Glasser, R.T. (2016). Deep learning as a tool to distinguish between high orbital angular momentum optical modes. *Proceedings SPIE*, 9970, 997013. <https://doi.org/10.1117/12.2242115>
- [19] Frączek, E., Popiołek-Masajada, A., & Szczepaniak, S. (2020). Characterization of the Vortex Beam by Fermat’s Spiral. *Photonics*, 7(4), 102. <https://doi.org/10.3390/photonics7040102>
- [20] Plocinniczak, Ł., Popiołek-Masajada, A., Masajada, J., & Szatkowski, M. (2016). Analytical model of the optical vortex microscope. *Applied Optics*, 55(12), B20–B27. <https://doi.org/10.1364/AO.55.000B20>
- [21] Popiołek-Masajada, A., Masajada, J., & Szatkowski, M. (2018). Internal scanning method as unique imaging method of optical vortex scanning microscope. *Optics and Laser in Engineering*, 105, 201–208. <https://doi.org/10.1016/j.optlaseng.2018.01.016>

- [22] Popiołek-Masajada, A., Masajada, J., & Kurzynowski, P. (2017). Analytical model of the optical vortex scanning microscope with the simple phase object. *Photonics*, 4(2), 38. <https://doi.org/10.3390/photonics4020038>
- [23] Takeda, T. M., Ina, H., Kobayashi, S. (1982). Fourier-transform method of fringe-pattern analysis for computer-based topography and interferometry. *Journal of the Optical Society of America*, 72(1), 156–60. <https://doi.org/10.1364/JOSA.72.000156>
- [24] Larkin, K. G., Bone, D. J., & Oldfield, M. A. (2001). Natural demodulation of two-dimensional fringe patterns. I.General background of the spiral phase quadrature transform. *Journal of the Optical Society of America A*, 18(8), 1862–1870. <https://doi.org/10.1364/JOSAA.18.001862>
- [25] Frączek, E., & Idźkowski, W. (2020). Artificial intelligent methods for the location of vortex points. In Rutkowski, L., Scherer, R., Korytkowski, M., Pedrycz, W., Tadeusiewicz R., & Zurada, J. M. (Eds.). *Artificial Intelligence and Soft Computing* (pp. 71–77). Springer. https://doi.org/10.1007/978-3-030-61401-0_7



Agnieszka Popiołek-Masajada received the Ph.D. degree in physics from Wrocław University of Technology in 1999. She is currently Assistant Professor at the Department of Optics and Photonics at Wrocław University of Science and Technology. She is co-author of over 30 journal and 30 conference publications. Her current scientific research interests include possible application of optical vortices to metrological purposes.



Emilia Burnecka received the B.Sc. degree in biomedical engineering (specializing in medical optics) from Wrocław University of Science and Technology (WUST), Poland (2019). She is currently a master's student of Optics and Photonics at WUST. Results presented in this manuscript are part of her Master's thesis.



Ewa Frączek received the Ph.D. degree in optics from Wrocław University of Technology in 2006. She is an Assistant Professor at the Department of Telecommunication and Teleinformatics at Wrocław University of Science and Technology. Her research activity focuses on metrological aspects of experimental methods and data analysis algorithms.